

# Hybrid Piezo/Triboelectric-Driven Self-Charging Electrochromic Supercapacitor Power Package

Shanshan Qin, Qian Zhang, Xixi Yang, Mengmeng Liu, Qijun Sun,\* and Zhong Lin Wang\*

The rapid development of personal electronics imposes a great challenge on sustainable and maintenance-free power supplies. The integration of nanogenerators (NG) and electrochromic supercapacitors (SC) offers a promising solution to efficiently convert mechanical energy to stored electrical energy in a predictable and noticeable manner. In this paper, by integrating hybrid NGs and electrochromic micro-SCs ( $\mu$ -SCs) array, the authors demonstrate a smart self-charging power package capable of indicating the charging state with color change. The electrochromic  $\mu$ -SC employs Ag nanowires/NiO as electrode materials, exhibiting high capacitance ( $3.47 \text{ mF cm}^{-2}$ ) and stable cycling performance (80.7% for 10000 cycles). The hybrid NG can produce a high output voltage of 150 V and an enhanced output current of  $20 \mu\text{A}$  to satisfy the self-charging requirements. The integrated electrochromic  $\mu$ -SCs array is capable of self-charging to 3 V to light up a LED under human palm impact. The charging states can be estimated according to the color differences with the naked eye during the self-charging process. Moreover, it is possible to design the planar interdigitated electrodes into different shapes according to user demand. The proposed simple and cost-effective approaches for smart self-charging power package may pave the way for future intelligent, independent and continuous operation of daily electronics.

With the rapid development of portable electronics, wearable sensors, and micro-electromechanical systems, technologies and energy supply for sustainable and maintenance-free operation of the intelligent devices are imperative.<sup>[1–3]</sup> At present, the mainstream power supply for electronic devices relies on rechargeable batteries, accompanying with some problems such as heavy weight, difficulty to be recycled, potential environmental pollution, and explosion risk.<sup>[4]</sup> Energy harvesting with nanogenerators (NGs) from ambient environment and regular human motions in low frequency integrated with energy storage devices may offer a safe, efficient, and environment-friendly way to power portable electronics.<sup>[5–9]</sup>

Both piezoelectric and triboelectric nanogenerators have been demonstrated to be significant energy sources and building blocks for self-powered systems. The combination of piezoelectric and triboelectric NGs is favorable to increase energy conversion efficiency according to their similar output properties, matched impedance, and simple fabrication process.<sup>[10–12]</sup> Among the energy storage devices, supercapacitor (SC) has been widely studied due to its high capacitance and power density, long cycle life, superior rate capability, and low cost.<sup>[13–17]</sup> Integration of NGs and SCs into a self-charging power package has been intensively investigated as sustainable power supply for electronic devices. However, it is impossible to visually determine the self-charging SCs are fully charged or consumed out before a device stops working. Combining the self-charging and electrochromic capability in power package makes it respond to the changes in a predictable and noticeable manner, which will

not only improve the self-charging efficiency but also prevent the power package from overcharging. Hence, to develop a self-charging power package capable of indicating the charging state may bring a lot of convenience to promote widespread applications of self-powered systems.

Electrochromism represents reversible color change upon applied voltage according to electrochemical redox reactions in the electrochromic materials.<sup>[18–20]</sup> Utilization of electrochromic materials as the electrode materials in supercapacitors has been demonstrated as wearable smart energy textile, bifunctional supercapacitors, and energy-storage smart windows, combining the advantages of energy storage and visual indication of the

S. Qin, Q. Zhang, X. Yang, M. Liu, Prof. Q. Sun, Prof. Z. L. Wang  
Beijing Institute of Nanoenergy and Nanosystems  
Chinese Academy of Sciences  
Beijing 100083, P. R. China  
E-mail: sunqijun@binn.cas.cn; zhong.wang@mse.gatech.edu

S. Qin, Q. Zhang, X. Yang, M. Liu, Prof. Q. Sun, Prof. Z. L. Wang  
School of Nanoscience and Technology  
University of Chinese Academy of Sciences  
Beijing 100049, P. R. China

S. Qin  
Institute of Semiconductors  
Chinese Academy of Sciences  
Beijing 100083, P. R. China  
Prof. Q. Sun, Prof. Z. L. Wang  
Center on Nanoenergy Research  
School of Physical Science and Technology  
Guangxi University  
Nanning 530004, China

Prof. Z. L. Wang  
School of Materials Science and Engineering  
Georgia Institute of Technology  
Atlanta, GA 30332-0245, USA

 The ORCID identification number(s) for the author(s) of this article can be found under <https://doi.org/10.1002/aenm.201800069>.

DOI: 10.1002/aenm.201800069

charging state.<sup>[21–26]</sup> The charge injection and extraction during the charging–discharging processes of the supercapacitor are consistent with the chromatic transitions under different potentials, which can efficiently indicate the energy storage levels. Nickel oxide (NiO) exhibits outstanding performance as the active electrode materials in both SCs and electrochromic devices.<sup>[27,28]</sup> Hydrothermal reaction is a low-cost and efficient method to synthesize NiO electrode materials with uniform nanostructures and high surface area, which facilitates electrolyte penetration and improves the specific surface capacitance.<sup>[29–33]</sup> Micro-supercapacitors ( $\mu$ -SCs) with interdigitated electrodes benefit from ready and rapid transport of the electrolyte ions through the narrow interspaces, exhibiting ultrahigh power capability. Planar geometry and avoidance of the separator also simplify the fabrication process and facilitate its integration with energy harvesting devices.

Here, we first demonstrated a flexible, compact, and smart self-charging power package capable of indicating the charging state with color change by integrating hybrid tribo/piezoelectric NG and solid-state electrochromic  $\mu$ -SCs array. The electrochromic  $\mu$ -SC employed Ag nanowires/NiO (AgNWs/NiO) on interdigitated indium tin oxide (ITO) electrodes as the active electrode materials, representing both high capacitance ( $3.47 \text{ mF cm}^{-2}$ ,  $17.4 \text{ F g}^{-1}$ ) and stable cycling performance (80.7% for 10 000 cycles). The hybrid NG was composed of a piezoelectric NG sharing the same silver electrode with a triboelectric NG, which produced a high output voltage of 150 V and an enhanced output current of 20  $\mu$ A. During the charging–discharging process, one of the interdigitated electrodes in  $\mu$ -SC turned to dark color and recovered to be transparent due to the reversible Faradaic redox process of  $\text{Ni}^{2+}/\text{Ni}^{3+}$  couple. Higher potential of the  $\mu$ -SC electrodes led to darker color, indicating a more charging state of the  $\mu$ -SC. The AgNWs/NiO electrodes showed high coloration efficiency ( $51.9 \text{ cm}^2 \text{ C}^{-1}$  at 550 nm) and excellent performance in reversible and reliable electrochromic behaviors. The integrated electrochromic  $\mu$ -SCs array could be self-charged to 3 V in 900 s to light up a light-emitting diode (LED) under a periodic mechanical deformation by human palm impact. The charging states could be estimated according to the color differences with naked eyes during the self-charging process. Moreover, the planar interdigitated electrodes could be designed into different shapes according to user demand. The proposed simple and cost-effective approaches for smart self-charging power package may pave the way for future intelligent, independent, and continuous operation of daily electronics.

The schematic illustration of the smart self-charging power package is depicted in **Figure 1a**, which contains two primary components: an electrochromic  $\mu$ -SCs array based on AgNWs/NiO active electrode materials and an arch-shaped hybrid tribo/piezoelectric NG (photo image in **Figure 1c**). The electrochromic  $\mu$ -SCs array consists of nine electrochromic  $\mu$ -SCs (three  $\mu$ -SCs are connected in parallel, and the parallel connected devices are connected in series). One electrochromic  $\mu$ -SC contains five pairs of interdigitated microelectrodes, including five positive and negative electrodes, respectively. The top inset in **Figure 1a** shows the illustration of a charged electrochromic  $\mu$ -SC. After charging, NiO is oxidized to NiOOH and shows a dark color on one of the interdigitated

electrodes, while the other electrode stays transparent. The hybrid NG (bottom inset in **Figure 1a**) consists of a piezoelectric NG with ITO/P(VDF-TrFE)/silver structure and a contact–separation mode triboelectric NG with silver/PTFE/silver structure (P(VDF-TrFE) and PTFE are the abbreviations of poly(vinylidene fluoride-co-trifluoroethylene) and polytetrafluoroethylene, respectively). Two NGs are vertically stacked into an arched shape, sharing the same silver electrode. To efficiently couple the piezoelectric and triboelectric charges, the bottom electrode of piezoelectric NG is used as the driving electrode for triboelectric NG.

**Figure 1b** shows the fabrication and electrochromic processes of the electrochromic  $\mu$ -SC. First, the interdigitated ITO microelectrodes were patterned by typical photolithography and acid etching processes.<sup>[34]</sup> The precursor ( $\text{AgNWs}/\text{Ni}(\text{OH})_2$ ) for the active electrode materials was directly grown on the patterned ITO electrodes through hydrothermal process and annealed at 350 °C for 60 min to form uniform AgNWs/NiO nanostructures. The electrolyte gel (poly(vinyl alcohol)/potassium hydroxide (PVA/KOH)) was coated on the active area of the device to assemble the electrochromic  $\mu$ -SC (detailed procedures given in the Experimental Section). The electrochromic  $\mu$ -SC can be efficiently charged by the hybrid NG through harvesting ambient mechanical energy. After charging, the positive electrodes turned to dark color due to the oxidation of NiO into NiOOH (the detailed mechanism will be discussed below).

Prior to studying the electrochemical performance of  $\mu$ -SC, the surface morphology of AgNWs/NiO active materials was investigated by scanning electron microscope (SEM) (**Figure 1d**). NiO film with 3D porous structures was uniformly grown on the glass substrate with interdigitated ITO electrodes. The AgNWs within the NiO framework intercrossed in multiple directions, formed proper intervals among the adjoining nanostructures and enhanced the conductivity. Thus, the prepared AgNWs/NiO electrode materials with porous structures would be accessible to the electrolyte and facilitate the reversible faradic reactions due to the presence of more ion diffusion paths. This was evidenced by the impedance analysis and capacitance characterization of AgNWs/NiO and pure NiO electrode materials, respectively. Apparently, specific surface capacitance of the electrochromic  $\mu$ -SC with AgNWs/NiO active electrode materials was higher than that with pure NiO (**Figure S1b,c**, Supporting Information) because the charge transfer resistance ( $R_{ct}$ ) of AgNWs/NiO electrode material (represented by the diameter of semicircle in the high-frequency region) was lower than pure NiO, indicating AgNWs additives contributed to improve the conductivity of the electrode (**Figure S1a**, Supporting Information). The inset of **Figure 1d** shows a high-magnification SEM image of the AgNWs/NiO nanostructures, representing large specific surface areas of the 3D porous structure. It would provide enormous electroactive sites of the outer branches to improve the utilization of the active material for high electrochemical performance. The phase information of NiO was characterized by X-ray diffraction (XRD) measurement (**Figure 1e**). To minimize the impact of the AgNW additives, XRD was conducted on control samples with only NiO electrodes. The diffraction peaks at  $2\theta$  degrees of  $37.8^\circ$ ,  $43.3^\circ$ , and  $62.7^\circ$  were assigned to (111), (200), and (220) crystal faces of the cubic NiO phase (JCPDS NO.: 65-5745), respectively.

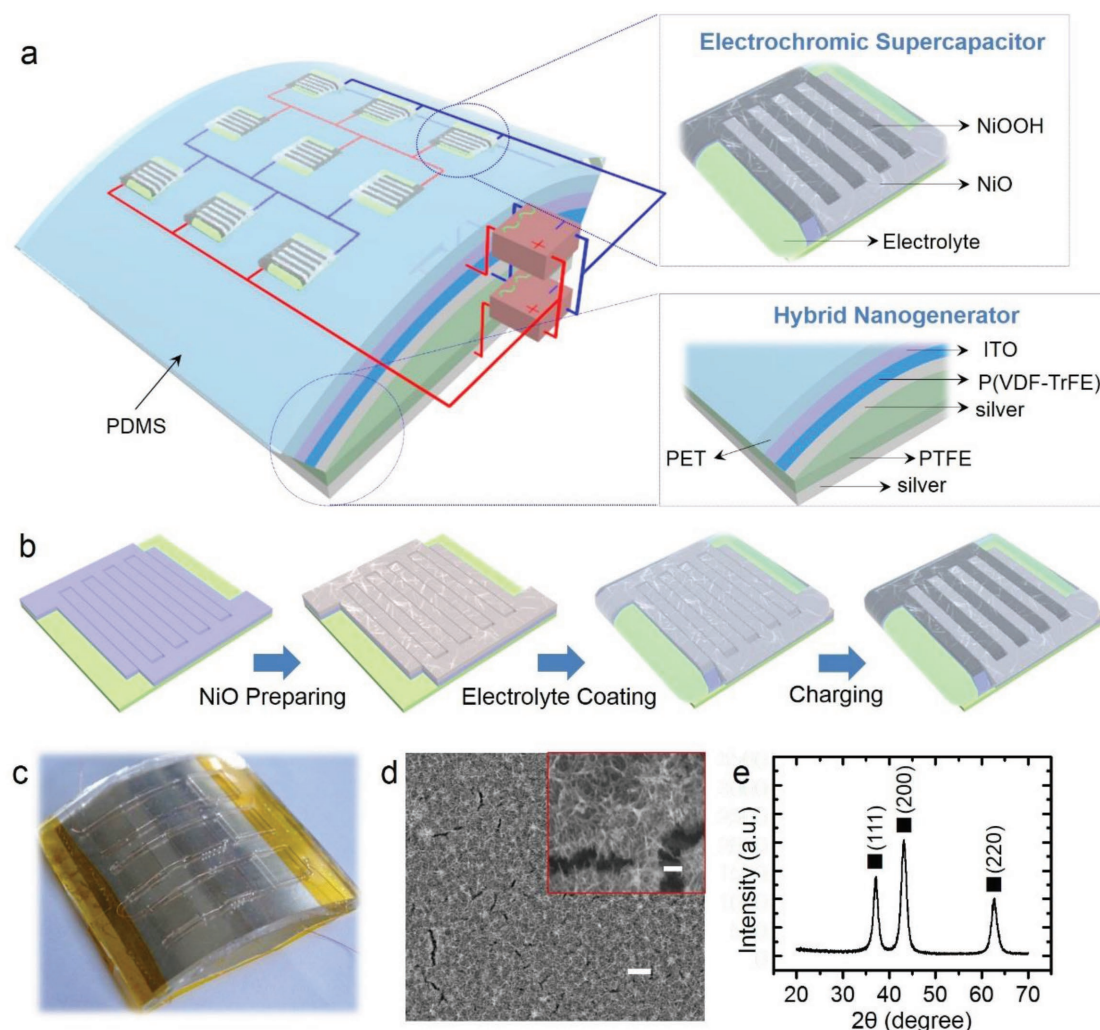


**Figure 1.** a) Schematic illustration of the self-charging power package. Top inset shows the structure of electrochromic  $\mu$ -SC; bottom inset shows the structure of hybrid NG. b) Fabrication and electrochromic process of the electrochromic  $\mu$ -SC. c) Photo image of the self-charging power package. d) SEM image of the AgNWs/NiO active electrode materials. The scale bar is 5  $\mu\text{m}$ . Inset is the enlarged SEM image. The scale bar is 100 nm. e) XRD pattern of the NiO scraped off from the substrate.

The results correlated well with previous studies,<sup>[35,36]</sup> which implied that the calcination temperature of 350  $^{\circ}\text{C}$  was sufficient to convert the precursor to pure NiO completely without any impurity peaks.

To evaluate the electrochemical performance of the electrochromic  $\mu$ -SC based on AgNWs/NiO nanocomposites, cyclic voltammetry (CV) and galvanostatic charge–discharge (GCD) measurements were conducted, respectively. **Figure 2a** shows the typical CV curves between 0 and 1 V at various scan rates ranging from 10 to 100  $\text{mV s}^{-1}$ . A pair of distinct redox peaks was observed in each cycle, indicating the existence of electrochemical redox reactions (i.e., the reversible Faradaic redox process of  $\text{Ni}^{2+}/\text{Ni}^{3+}$  couple,  $\text{NiO} + \text{OH}^- \rightleftharpoons \text{NiOOH} + \text{e}^-$ ). **Figure 2b** shows the GCD curves of the electrochromic  $\mu$ -SC under various current densities ranging from 20 to 100  $\mu\text{A cm}^{-2}$  in the potential from 0 to 1 V. The specific surface capacitances calculated from the GCD curves at different current densities are shown in **Figure 2c**. The areal discharge capacitance

at 2  $\mu\text{A cm}^{-2}$  was determined to be 3.47  $\text{mF cm}^{-2}$ , which remained to be 0.91  $\text{mF cm}^{-2}$  after increasing the current density 10 times up to 20  $\mu\text{A cm}^{-2}$ . The corresponding specific capacitance was 17.4  $\text{F g}^{-1}$  (considering AgNWs/NiO electrode mass). It represented excellent capacitive behaviors of the  $\mu$ -SC under fast charge–discharge process. Good cyclic stability of the electrochromic  $\mu$ -SC employing AgNWs/NiO electrode was also observed in **Figure 2d**, retaining 80.7% of the initial capacitance after 10 000 charge/discharge cycles. Inset shows the GCD curve for the last 10 cycles of the charging–discharging process. The capacitance decay over 10 000 cycles was attributed to that some hydroxy groups ( $\text{OH}^-$ ) might penetrate into the electrode film during the electrochemical redox reactions and could not be extracted out completely. Cycling stability of the controlled sample with pure NiO electrode was also investigated in **Figure S2** (Supporting Information), retaining 85.4% of the initial capacitance after 10 000 charge/discharge cycles. A Ragone plot of the electrochromic  $\mu$ -SC with areal energy

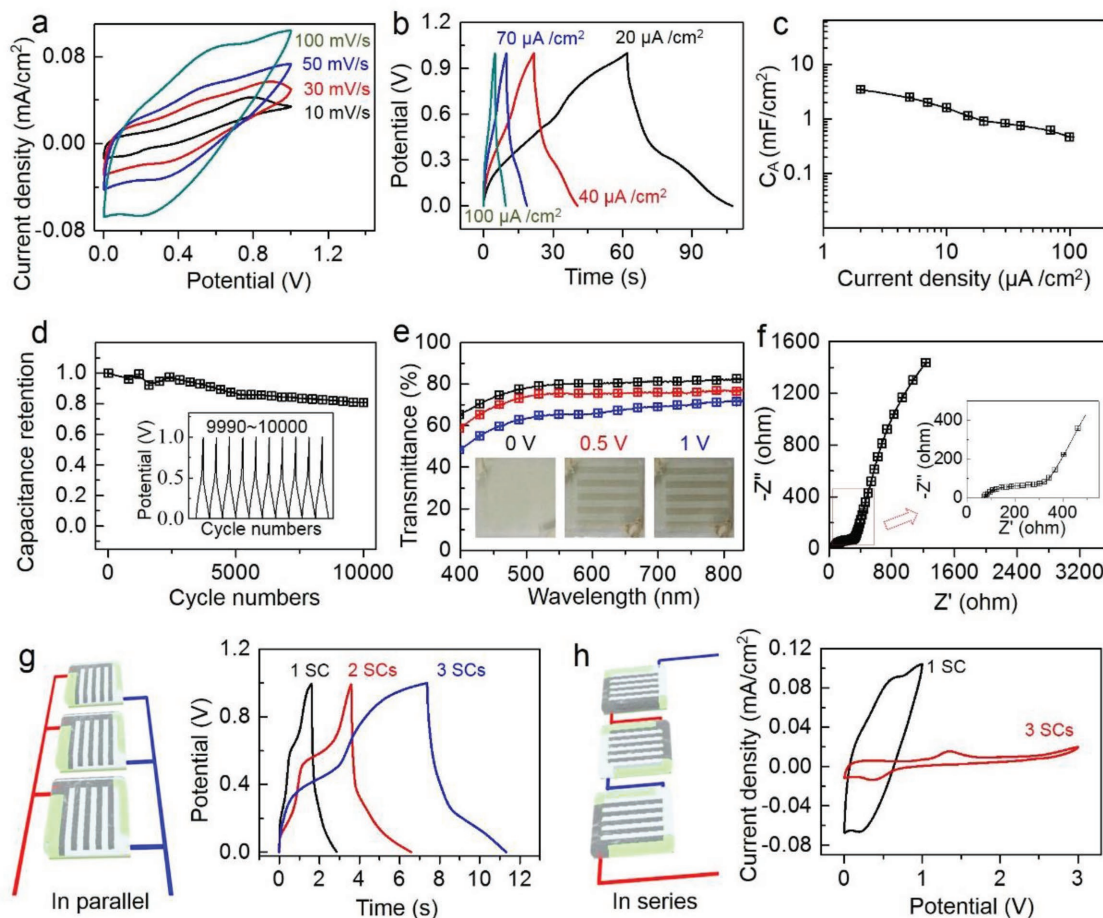


**Figure 2.** a) CV curves of the electrochromic  $\mu$ -SC at different scanning rates. b) GCD profiles at different current densities. c) Specific areal capacitances calculated from GCD curves. d) Cycling performance of the electrochromic  $\mu$ -SC at  $50 \mu\text{A cm}^{-2}$ . Inset shows the voltage profiles of the last 10 cycles. e) Transmittance spectra of the electrochromic  $\mu$ -SC under different charging states (0, 0.5, and 1 V). Insets are the corresponding photo images. f) Nyquist curve of the electrochromic  $\mu$ -SC. Inset is the enlarged view at the high-frequency region. g) GCD profiles of electrochromic  $\mu$ -SCs connected in parallel (one to three). Left panel shows the  $\mu$ -SCs connected in parallel. h) CV curves of one  $\mu$ -SC and three  $\mu$ -SCs connected in series. Left inset shows  $\mu$ -SCs connected in series.

density and power density is also provided in Figure S3 (Supporting Information) to better evaluate its commercial application potential.

The above results demonstrated that the AgNWs/NiO electrodes exhibited excellent capacitive properties. In addition, NiO has been demonstrated to have high electrochromic efficiency with good cyclic reversibility.<sup>[27,28]</sup> According to the reversible Faradaic redox process of  $\text{Ni}^{2+}/\text{Ni}^{3+}$  couple, positive and negative electrodes of the  $\mu$ -SC were envisioned to exhibit different colors at varied electrical potentials to indicate the charging state during the charging–discharging process. As shown in the inset of Figure 2e, the positive electrodes of the  $\mu$ -SC changed to gray color when the electrochromic  $\mu$ -SC was charged to 0.5 V. Upon fully charged to 1 V, the color of positive electrodes turned to be darker, while the negative electrode maintained transparent (Figure 2e). The transmittances of the electrochromic electrodes at a wavelength of 550 nm were 80.0, 75.1, and 65.7% at the charged states of 0, 0.5, and 1 V, respectively. More detailed transmittance variations and the extracted transmittances of the AgNWs/NiO electrodes under different

charging voltages at a wavelength of 550 nm are provided in Figure S4a,b (Supporting Information). We also investigated the electrochromic stability of the  $\mu$ -SC (the colored and bleached transmittance at 550 nm, Figure S5, Supporting Information). After 2000 electrochromic cycles, the electrochromic  $\mu$ -SC exhibited good electrochromic stability and could sustain the initial transmittance modulation ( $\approx 15\%$ ) even though the base transmittance was decreased by 84.1% (from 80.0% to 67.2% at the charging state). The possible reason for the degradation of the device transmittance may be attributed to the slight oxidation of AgNW additives after long-term cycles (2000 cycles). Before 2000 cycles, we considered there was no oxidation of AgNWs according to the good electrochromism and cycling performances (Figure 2d; Figure S5, Supporting Information). The absence of AgNWs oxidation before charging/discharging over 2000 cycles may be attributed to that the charging potential drop mainly functionalizes on high resistance NiO but not the highly conducting AgNWs joints. Long-term charging cycles increased the potential drop time on AgNWs and led to the slight oxidation.

Coloration efficiency ( $\eta$ ) is an important parameter to qualify the electrochromism performance, defined as  $\eta = \log(T_b/T_c)/\Delta Q$ , where  $\Delta Q$  is the unit charge intercalated into the electrochromic materials at certain wavelength,  $T_b$  and  $T_c$  denote transmittance in bleached and colored states, respectively. The coloration efficiency is  $51.9 \text{ cm}^2 \text{ C}^{-1}$  at 550 nm for the porous AgNWs/NiO nanostructures. The color variation under different charging state depended on the oxidation amount of transparent NiO participating in the electrochemical reaction:  $\text{NiO} + \text{OH}^- \rightleftharpoons \text{NiOOH} + \text{e}^-$ . The oxidation of more  $\text{Ni}^{2+}$  (NiO, transparent) to  $\text{Ni}^{3+}$  (NiOOH, non-transparent) resulted in the darker color of the electrodes, indicating the more charges were stored. More detailed color variations under different charging states are provided in Figure S6 (Supporting Information). The transmittance differences of the electrochromic electrodes were sufficient enough to distinguish the charging states. Further improvement on the electrochromic performance is available by preparing porous NiO films hybrid with other nanomaterials (e.g., reduced graphene oxide).<sup>[37]</sup> When the electrochromic  $\mu$ -SC was discharged to 0 V, the positive electrodes were bleached to the original transparent state (Figure S7, Supporting Information), confirming good reversibility of the electrochromic transitions. By contrast, the negative electrode turned to dark color while positive electrode remained transparent after charging in an opposite voltage (−1 V), as shown in Figure S8 (Supporting Information). This was because the oxidation of NiO to NiOOH occurred on the negative electrodes, resulting in the color change on the negative electrodes. Thus, the electrochromic  $\mu$ -SC was able to indicate both the charging intensities and charging directions, which was convenient to be utilized for powering portable electronics.

To further understand the electrochemical behavior and the electrochemical compatibility of the AgNWs/NiO active electrode materials, electrochemical impedance spectrum was applied in a frequency range from 0.01 Hz to 100 kHz at an open-circuit potential of 5 mV (Figure 2f). The equivalent series resistance was calculated as  $74.7 \ \Omega$  according to the inset of Figure 2f (magnified plot in the high frequency range), indicating the electrochromic  $\mu$ -SC with good ionic response at high frequency range. The small resistance reflected the excellent conductivity of the AgNWs/NiO electrodes, which also contributed to the small voltage drop in the GCD curve. In the low frequency range, the Nyquist plot represented an inclined line with large slope, indicating ideal capacitive behavior of the device.

In order to satisfy the specific energy requirements for higher voltage or capacitance in practical applications, multiple electrochromic  $\mu$ -SCs based on AgNWs/NiO active electrode materials can be connected in series or parallel. As shown in Figure 2g, when the electrochromic  $\mu$ -SCs were connected in parallel (two or three devices), the charge/discharge time for the parallel connected devices (at a voltage window of 1 V) was increased by two or three times more than that of a single device, respectively. This indicated the increased capacitance in the parallel connected  $\mu$ -SCs. In the case of three  $\mu$ -SCs connected in series, the CV voltage window was increased to 3 V, three times higher than that of a single device (Figure 2h). The higher capacitance and larger operating voltage window achieved in the  $\mu$ -SCs by simple parallel and serial connections

could facilitate their practical applications as energy storage devices.

To ensure the feasibility of the self-charging process in the proposed device's structure, an energy-harvesting component with high-output power is essential. A hybrid piezo/triboelectric NG combining the high voltage output of triboelectric NG<sup>[38]</sup> and high current output of piezoelectric NG<sup>[39,40]</sup> was employed as the charging component in the electrochromic power package (bottom inset in Figure 1a). The piezoelectric and triboelectric NGs are vertically stacked into an arch-shape, with a same silver electrode as sharing electrode. Under the continuous palm impact at low frequency, the hybrid piezo/triboelectric outputs were simultaneously produced in one press-and-release cycle.<sup>[10]</sup> Figure S9 (Supporting Information) illustrates the detailed operating mechanism for the hybrid NG. At the original state (Figure S9a, Supporting Information), both the piezoelectric and triboelectric NGs stayed in the charge-balance state without any voltage outputs. When it was subjected to the palm impact, piezopotential was enhanced in the P(VDF-TrFE) layer and drove the electrons to flow from the "Silver 1" to top ITO electrode. Meanwhile, the electrostatic induction effect between "Silver 1" electrode and PTFE film was gradually enhanced and more electrons were attracted on the surface of PTFE layer, exhibiting electrons transfer from "Silver 1" to bottom "Silver 2" electrode through external circuit. When the top NG fully contacted with PTFE layer (Figure S9c, Supporting Information), both the piezoelectric and triboelectric output voltages reached the maximum peak value. When the palm impact was released (Figure S9d, Supporting Information), the arch-structure started to bounce back. The electrons driven by both piezoelectric and triboelectric NGs flowed back to the shared "Silver 1" electrode from top ITO and bottom "Silver 2" electrodes, respectively. Notably, to ensure the shared "Silver 1" electrode as the starting (or terminal) point for the transferred electrons, the P(VDF-TrFE) layer was required to be polarized in a downward direction (dipoles distribution as shown in Figure S9b, Supporting Information) to match with the charges distribution induced by the electrostatic induction between "Silver 1" electrode and PTFE layer. Two bridge rectifiers were required to convert the hybrid piezo/triboelectric alternating current pulses to direct currents.

Figure 3a,b shows the rectified hybrid open-circuit voltages and short-circuit currents of the hybrid NG under continuous palm impact. This hybrid NG combined both the advantages of high output current in piezoelectric NG and high output voltage in triboelectric NG. As shown in Figure 3a, the rectified hybrid output voltage showed an average peak value over 150 V, higher than both the rectified piezoelectric and triboelectric output voltage (Figure S10a,c, Supporting Information). An average peak value exceeding 20  $\mu\text{A}$  for the rectified short-circuit current was observed, also higher than both the rectified piezoelectric and triboelectric output current (Figure S10b,d, Supporting Information). During the vertical contact–separation process of the hybrid NG, the transfer charge density ( $\Delta\sigma$ ) driven by the hybrid piezo/triboelectric potential was measured to be  $\approx 55 \ \mu\text{C m}^{-2}$  (Figure 3c). Figure 3d illustrates the dependence of the voltage outputs and electrical power densities on a series of different resistances (from  $10^3$  to  $10^9 \ \Omega$ ). The voltages were drastically increased with the increased

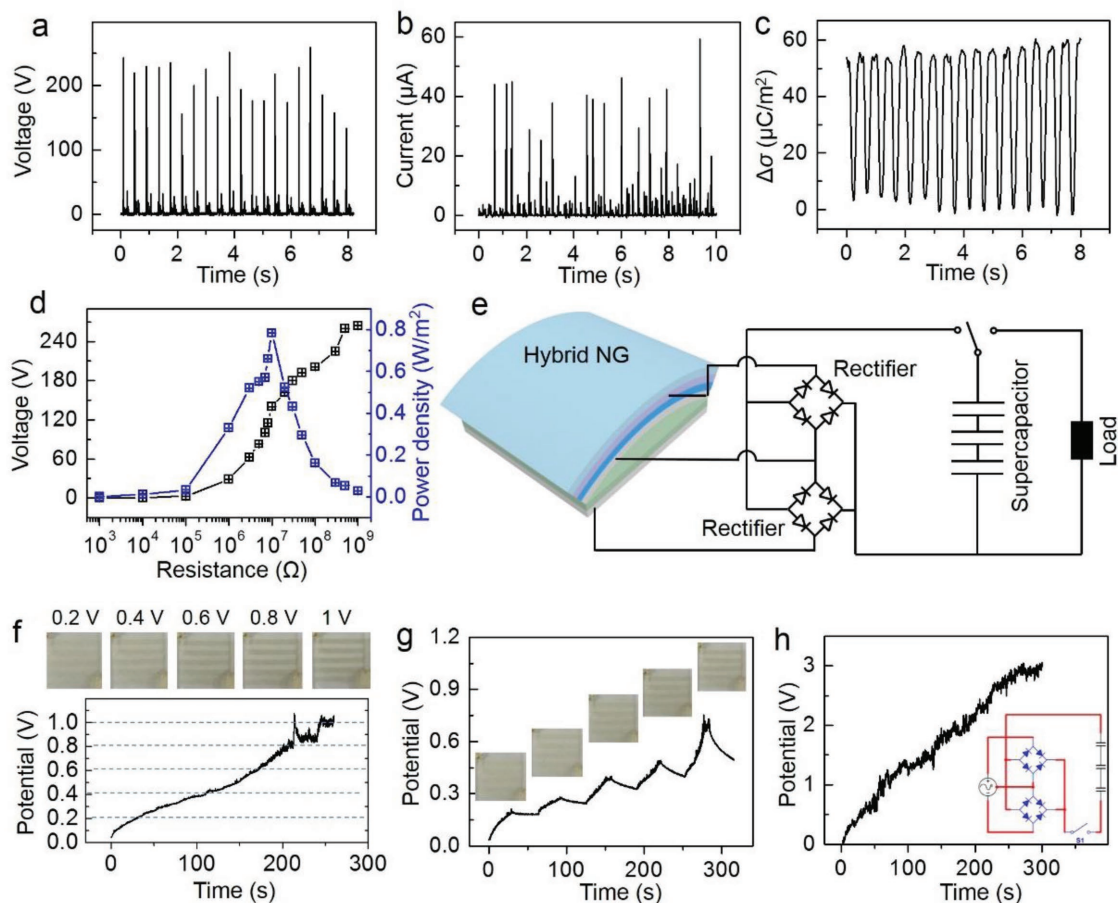


**Figure 3.** a) Rectified open-circuit voltage, b) rectified short-circuit current, and c) transferred charge density ( $\Delta\sigma$ ) generated by the hybrid NG under palm impact. d) The dependence of the output voltage and power density of the hybrid NG on the resistance of external load. e) The equivalent circuit of the smart self-charging power package. f) The real-time charged voltage of electrochromic  $\mu$ -SC by the hybrid NG under palm impact. Top panels show the corresponding chromatic transitions of a  $\mu$ -SC at different voltages. g) The real-time self-charging process of the electrochromic  $\mu$ -SC under continuous palm impact. Insets are the chromatic transitions of a  $\mu$ -SC at different self-charging states. h) Three electrochromic  $\mu$ -SCs connected in series charged by the hybrid NG under continuous palm impact. Inset is the equivalent circuit.

external resistances. The effective electrical power densities of the hybrid generator calculated from the output voltages were closely related with the external load, reaching the maximum value ( $0.8 \text{ W m}^{-2}$ ) at a load resistance of  $10^7 \Omega$ . The equivalent circuit of the self-charging electrochromic  $\mu$ -SCs was shown in Figure 3e. Two bridge rectifiers were used to rectify the current for charging the electrochromic  $\mu$ -SCs.

To demonstrate the indication capability of the charging state during self-charging process in real-time, the self-charging process was conducted under continuous palm impact, and the color variation of the electrochromic  $\mu$ -SC was recorded. When the continuous palm impact was applied to charge the electrochromic  $\mu$ -SC, the voltage of the device was increased from 0.05 to 1 V (charged by 0.95 V) in 260 s (Figure 3f). Top panels in Figure 3f represent the corresponding color variation of the interdigitated electrodes at different charging states. The electrodes color turned to be darker at higher charging state. As shown in Figure 3g, the real-time self-charging process of the electrochromic  $\mu$ -SC was characterized. The charged voltage of the  $\mu$ -SC was gradually increased under the continuous palm impact for 30 s, and the color change of the electrodes was

recorded at the same time. The charged voltage of  $\mu$ -SC sustained at 0.15 V in the first 30 s after stopping the palm impact. When the palm impact was applied again, the  $\mu$ -SC restarted to be self-charged with darker color change to indicate the relevant charging state. After all the self-charging process, the device could sustain the charged voltage for around 30 s. To achieve higher voltage, three electrochromic  $\mu$ -SCs connected in series were able to be charged to 3 V (within 300 s) with the hybrid NG under continuous palm impact (Figure 3h).

To demonstrate the potential application of the self-charging electrochromic  $\mu$ -SCs as power package, we assembled nine electrochromic  $\mu$ -SCs (three  $\mu$ -SCs were connected in parallel, and the parallel connected devices were connected together in series) and used those to drive a LED (Figure 4a). The  $\mu$ -SCs as the power source were charged to the required operating voltage of the LED by using the hybrid NG with rectifiers. As shown in Figure 4b, the potential of the assembled device during the self-charging process was recorded in real-time.

The indication function of the charging state with the electrochromic  $\mu$ -SCs was also characterized. According to the planar structure of electrochromic  $\mu$ -SC, the shapes of interdigitated

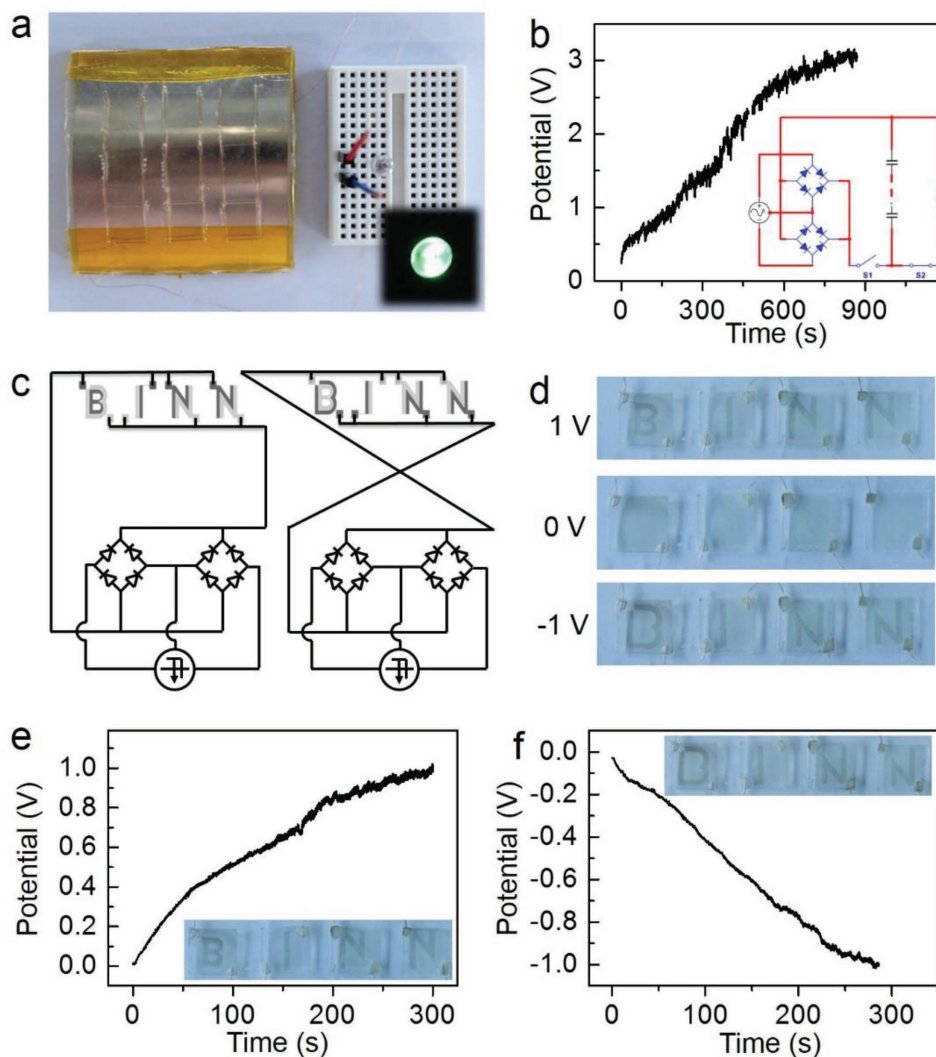


**Figure 4.** a) The self-charging electrochromic power package as the power source to light a LED. b) Self-charged voltage of the assembled nine electrochromic  $\mu$ -SCs by the hybrid NG. c) The equivalent circuit of forward and reverse connections of “BINN”-shaped electrochromic  $\mu$ -SCs with a hybrid NG. d) Chromatic transitions of the “BINN”-shaped  $\mu$ -SCs at different voltages (charged by the electrochemical workstation). e,f) “BINN”-shaped electrochromic  $\mu$ -SCs were self-charged to 1 and  $-1$  V, respectively. Insets show the photograph of the  $\mu$ -SCs self-charged to 1 and  $-1$  V, respectively.

electrodes were facile to be designed on demand. To demonstrate a practical application, the microelectrodes in the logo shape of “BINN” (representing Beijing Institute of Nanoenergy and Nanosystems) were patterned with inner and outer counter electrodes, as shown in Figure 4c. Then the designed electrochromic  $\mu$ -SCs were connected in parallel and charged under both the forward and reverse connections, respectively. Two bridge rectifiers were utilized to convert the alternating current pulses generated by the tribo/piezoelectric hybrid NG to a direct current. Before verifying the indication ability of the self-charging power package, the parallel connected  $\mu$ -SCs in “BINN” shapes were first charged by an electrochemical workstation to ensure the normal operation. As shown in Figure 4d, electrochromic behaviors were observed at both charging (1 V) and reverse charging states ( $-1$  V). When the electrochromic  $\mu$ -SCs were positively charged to 1 V, a smaller “B” (inner patterned electrodes) appeared due to the oxidation of NiO to

NiOOH on the inner microelectrodes. By contrast, when the electrochromic  $\mu$ -SCs were negatively charged to  $-1$  V, a bigger “B” (outer patterned electrodes) with dark color appeared due to the oxidation occurring on the outer microelectrodes. Other alphabets (“I” and “N”) also represented corresponding color change on reverse electrodes at different charging directions. Without charging (0 V), the  $\mu$ -SCs logo was transparent as no oxidation of NiO occurred. Figure S11 (Supporting Information) shows the CV and GCD measurement results charged by the electrochemical workstation for the forward and reverse connections.

The self-charging state was then verified by charging the electrochromic  $\mu$ -SCs (“BINN” shape) under continuous palm impact. As shown in Figure 4e, real-time self-charging process of the “BINN”-shaped  $\mu$ -SCs was monitored. Inset shows smaller alphabets presented in dark color, indicating the  $\mu$ -SCs were in a positively charged state (1 V). As shown in Figure 4f,

bigger alphabets were observed when the electrochromic  $\mu$ -SCs were negatively self-charged to  $-1$  V. More detailed color variations of the self-charged BINN at different charged states are provided in Figure S12 (Supporting Information). All those results showed that the smart self-charging electrochromic power package was capable of indicating the charging state with color change.

In conclusion, a self-charging electrochromic power package capable of indicating the charging state was demonstrated. Hybrid piezo/triboelectric NG with high output power was integrated with the electrochromic micro-supercapacitors with excellent electrochemical properties to achieve the compact and smart self-charging power package. It enabled reversible and stable chromatic transitions under different charging stages, providing sufficient information on their working status in real time. Self-charging process was efficiently conducted under continuous palm impact. Thanks to the planar structure of  $\mu$ -SCs, the electrodes can be designed into arbitrary shapes according to user's demand. Although monotonous colors of light gray and dark gray were demonstrated in this work, more diverse colors can be realized by utilizing other electrochromic materials as the active electrodes in  $\mu$ -SCs. Therefore, the indication function of the device could be diversified to satisfy more complicated situations. According to the electrochromic behaviors under external mechanical motion, it is possible to develop self-charging interactive displays, touch screens, electronic tags, etc. This work may promote the development of intelligent and sustainable self-powered systems. Combination of energy harvesting, energy storage, and indication functional devices still pursues the development of high output power densities, large capacitances, fast charging capability, and high flexibility in future.

## Experimental Section

**Preparation of the Solid-State Electrochromic  $\mu$ -SC:** Commercial ITO-coated glass ( $1 \times 1 \text{ cm}^2$ ) was first cleaned in acetone, alcohol, and deionized (DI) water under ultrasonication, respectively. Subsequently, the interdigitated electrodes were patterned through typical photolithography and acid etching processes.<sup>[32]</sup> A single electrochromic  $\mu$ -SC contains five pairs of interdigitated microelectrodes, including five positive and negative electrodes, respectively. Each of the electrodes has a width and length of 0.7 and 7.8 mm, respectively. The space between positive and negative electrodes was 50  $\mu\text{m}$ . A photoresist mask (AZ5214) was patterned on the intervals of the interdigital electrodes to guarantee that the active electrode materials only grew on the interdigital electrodes. After hydrothermal growth of AgNWs/NiO electrodes, the photoresist mask was removed by acetone. To prepare the precursor of AgNWs/NiO electrode materials, 0.4375 g  $\text{Ni}(\text{NO}_3)_2 \cdot 6\text{H}_2\text{O}$ , 1.4583 g urea, and 2 mL ( $0.5 \text{ g L}^{-1}$ ) AgNWs were dissolved in 70 mL DI water to form a homogeneous absinthe-green solution. Then, the patterned ITO glass was vertically placed into a Teflon-lined stainless-steel autoclave. The autoclave was sealed and maintained at 120  $^\circ\text{C}$  for 12 h to prepare precursor ( $\text{AgNWs}/\text{Ni}(\text{OH})_2$ ), which was directly grown on the surface of patterned ITO glass. AgNWs/NiO nanostructures on the interdigital ITO electrodes were achieved after the hydrothermal reaction with subsequent annealing process (350  $^\circ\text{C}$  in air for 60 min). To prepare the PVA/KOH gel electrolyte, 3.58 g KOH (90 wt%, Aladdin) and 6 g poly (vinyl alcohol) powder (molecular weight (MW) = 200, Aladdin) were added to 60 mL DI water with continuous stirring at 95  $^\circ\text{C}$  until the solution became clear.

The obtained PVA/KOH electrolyte gel was coated on the active area of the device to achieve the electrochromic  $\mu$ -SC. In control experiment, the same amount of  $\text{Ni}(\text{NO}_3)_2 \cdot 6\text{H}_2\text{O}$  and urea without AgNWs were dissolved in DI water to prepare the NiO electrodes. Other processes to assemble the  $\mu$ -SC are the same.

**Fabrication Process of the Hybrid NG:** First, P(VDF-TrFE) solution (20 wt%) was prepared by dissolving the P(VDF-TrFE) powder in N, N-dimethylformamide (DMF) solvent. The solution was stirred over two days to obtain a uniform solution. And then the solution was spin-coated on the commercial polyethylene terephthalate (PET) substrate with ITO coating ( $6 \text{ cm} \times 6 \text{ cm}$ ) at 2000 rpm for 40 s, followed with drying at 60  $^\circ\text{C}$  for 10 min to remove the DMF solvent and subsequent annealing at 140  $^\circ\text{C}$  for 2 h in air to enhance the piezoelectric  $\beta$ -phase of the P(VDF-TrFE). After that, the silver electrode (100 nm) was thermally deposited on the surface of P(VDF-TrFE) film to achieve the piezoelectric NG. Then, the whole P(VDF-TrFE) NG was attached on the PTFE/Ag substrate (100 nm silver electrodes were thermally deposited on the back side of commercial PTFE film) with sealing at both ends of the substrate to achieve the arch-shape. The silver electrode deposited on P(VDF-TrFE) was used as the driving electrode for the bottom triboelectric NG.

**Assembling of Self-Charging Electrochromic  $\mu$ -SCs Power Package:** The electrochromic  $\mu$ -SCs array was attached on top of the hybrid NG. To make sure the electrochromic  $\mu$ -SCs array was steadily attached on the hybrid NG, the back side of PET film for P(VDF-TrFE) NG was first spin-coated with polydimethylsiloxane (PDMS) liquid precursor. Then the electrochromic  $\mu$ -SCs array was fixed on the partially cured PDMS and sealed with another PDMS layer. The PDMS adhesive and sealing layer was prepared by mixing the liquid PDMS elastomer (Sylgard 184, Dow corning) and a curing agent (in the ratio of 10:1 by weight).

**Characterization:** SEM images were taken with a Hitachi SU8020. XRD measurements were conducted by a Panalytical instrument (X'Pert 3 Powder). The transmittance was measured with a UV3600 spectrophotometer. For the transmittance test, the electrochromic  $\mu$ -SC with five pairs of interdigitated microelectrodes was immobilized in the UV-vis spectrophotometer with a solid sample holder, and the light spot penetrated through the whole device. The electrochromic  $\mu$ -SC was also connected to a charge/discharge instrument. The electrochemical performance was measured by an electrochemical work station (CHI 660E). All electrochemical performances of the devices were tested with PVA/KOH as solid electrolyte. The capacitances calculated from GCD discharging curves were derived from  $C_{\text{device}} = \frac{It}{U}$ , where  $I$  was the discharging current,  $t$  was the discharging time,  $U$  was the cutoff voltage (i.e., 1 V). The areal specific capacitance ( $C_A$ ) was defined as  $C_A = \frac{C_{\text{device}}}{A}$ , where  $A$  was the area of the device ( $1 \text{ cm}^2$ ). The areal energy density and power density were obtained by  $E_A = \frac{1}{2} \times C_A \times \frac{U^2}{3600}$  and  $P_A = \frac{3600 \times E_A}{t}$ , where  $t$  was the discharging time.

## Supporting Information

Supporting Information is available from the Wiley Online Library or from the author.

## Acknowledgements

This work was supported by the National Key Research and Development Program of China (grant nos. 2016YFA0202703 and 2016YFA0202704), the National Natural Science Foundation of China (grant nos. 51605034 and 51711540300), the "Hundred Talents Program" of the Chinese Academy of Science, and the "Thousand Talents" program of China for pioneering researchers and innovative teams.

## Conflict of Interest

The authors declare no conflict of interest.

## Keywords

electrochromic, hybrid nanogenerators, micro-supercapacitors, piezo/triboelectric, self-charging energy packages

Received: January 8, 2018

Revised: April 9, 2018

Published online:

- 
- [1] S. Lee, H. Seong, S. G. Im, H. Moon, S. Yoo, *Nat. Commun.* **2017**, *8*, 725.
- [2] Q. Sun, H. H. Dong, Y. Choi, C. Pan, D. H. Kim, L. W. Zhong, J. H. Cho, *ACS Nano* **2016**, *10*, 11037.
- [3] H. Bae, B. C. Jang, H. Park, S. H. Jung, H. M. Lee, J. Y. Park, S. B. Jeon, G. Son, I. W. Tcho, K. Yu, S. G. Im, S. Y. Choi, Y. K. Choi, *Nano Lett.* **2017**, *17*, 6443.
- [4] J. M. Tarascon, M. Armand, *Nature* **2001**, *414*, 359.
- [5] X. Pu, L. Li, M. Liu, C. Jiang, C. Du, Z. Zhao, W. Hu, Z. L. Wang, *Adv. Mater.* **2016**, *28*, 98.
- [6] H. Guo, M. H. Yeh, Y. C. Lai, Y. Zi, C. Wu, Z. Wen, C. Hu, Z. L. Wang, *ACS Nano* **2016**, *10*, 10580.
- [7] Y. Ma, Q. Zheng, Y. Liu, B. Shi, X. Xue, W. Ji, Z. Liu, Y. Jin, Y. Zou, *Z. An, Nano Lett.* **2016**, *16*, 6042.
- [8] J.-H. Lee, J. Kim, T. Y. Kim, M. S. Al Hossain, S.-W. Kim, J. H. Kim, *J. Mater. Chem. A* **2016**, *4*, 7983.
- [9] Q. Sun, W. Seung, B. J. Kim, S. Seo, S. W. Kim, J. H. Cho, *Adv. Mater.* **2015**, *27*, 3411.
- [10] W. S. Jung, M. G. Kang, H. G. Moon, S. H. Baek, S. J. Yoon, Z. L. Wang, S. W. Kim, C. Y. Kang, *Sci. Rep.* **2015**, *5*, 9309.
- [11] X. He, Y. Zi, H. Yu, S. L. Zhang, J. Wang, W. Ding, H. Zou, W. Zhang, C. Lu, Z. L. Wang, *Nano Energy* **2017**, *39*, 328.
- [12] G. Hassan, F. Khan, A. Hassan, S. Ali, J. Bae, C. H. Lee, *Nanotechnology* **2017**, *28*, 175402.
- [13] X. D. Zhuang, F. Zhang, D. Q. Wu, N. Forler, H. W. Liang, M. Wagner, D. Gehrig, M. R. Hansen, F. Laquai, X. L. Feng, *Angew. Chem., Int. Ed.* **2013**, *52*, 9668.
- [14] F. X. Wang, X. W. Wu, X. H. Yuan, Z. C. Liu, Y. Zhang, L. J. Fu, Y. S. Zhu, Q. M. Zhou, Y. P. Wu, W. Huang, *Chem. Soc. Rev.* **2017**, *46*, 6816.
- [15] Y. Ko, M. Kwon, W. K. Bae, B. Lee, S. W. Lee, J. Cho, *Nat. Commun.* **2017**, *8*, 536.
- [16] H. Y. Li, Y. Hou, F. X. Wang, M. R. Lohe, X. D. Zhuang, L. Niu, X. L. Feng, *Adv. Energy Mater.* **2017**, *7*, 1601847.
- [17] C. Q. Yang, K. S. Schellhammer, F. Ortmann, S. Sun, R. Dong, M. Karakus, Z. Mics, M. Loeffler, F. Zhang, X. D. Zhuang, E. Canovas, G. Cuniberti, M. Bonn, X. L. Feng, *Angew. Chem., Int. Ed.* **2017**, *56*, 3920.
- [18] Y. Zhong, Z. S. Chai, Z. M. Liang, P. Sun, W. G. Xie, C. X. Zhao, W. J. Mai, *ACS Appl. Mater. Interfaces* **2017**, *9*, 34085.
- [19] G. Cai, P. Darmawan, X. Cheng, P. S. Lee, *Adv. Energy Mater.* **2017**, *7*, 1602598.
- [20] L. X. Shen, L. H. Du, S. Z. Tan, Z. G. Zang, C. X. Zhao, W. J. Mai, *Chem. Commun.* **2016**, *52*, 6296.
- [21] T. G. Yun, D. Kim, Y. H. Kim, M. Park, S. Hyun, S. M. Han, *Adv. Mater.* **2017**, *29*, 1770231.
- [22] X. Xia, D. Chao, X. Qi, Q. Xiong, Y. Zhang, J. Tu, H. Zhang, H. J. Fan, *Nano Lett.* **2013**, *13*, 4562.
- [23] P. H. Yang, P. Sun, Z. S. Chai, L. H. Huang, X. Cai, S. Z. Tan, J. H. Song, W. J. Mai, *Angew. Chem., Int. Ed.* **2014**, *53*, 11935.
- [24] X. Chen, H. Lin, J. Deng, Y. Zhang, X. Sun, P. Chen, X. Fang, Z. Zhang, G. Guan, H. Peng, *Adv. Mater.* **2014**, *26*, 8126.
- [25] P. P. Zhang, F. Zhu, F. X. Wang, J. H. Wang, R. H. Dong, X. D. Zhuang, O. G. Schmidt, X. L. Feng, *Adv. Mater.* **2017**, *29*, 1604491.
- [26] C. Y. Yan, W. B. Kang, J. X. Wang, M. Q. Cui, X. Wang, C. Y. Foo, K. J. Chee, P. S. Lee, *ACS Nano* **2014**, *8*, 316.
- [27] J. P. Tu, J. Zhang, Y. J. Mai, Y. Lu, C. D. Gu, X. L. Wang, *Nanoscale* **2012**, *4*, 5724.
- [28] G. Cai, X. Wang, M. Cui, P. Darmawan, J. Wang, A. L.-S. Eh, P. S. Lee, *Nano Energy* **2015**, *12*, 258.
- [29] T. Liu, C. J. Jiang, B. Cheng, W. You, J. G. Yu, *J. Power Sources* **2017**, *359*, 371.
- [30] M. X. Liu, X. Wang, D. Z. Zhu, L. C. Li, H. Duan, Z. J. Xu, Z. W. Wang, L. H. Gan, *Chem. Eng. J.* **2017**, *308*, 240.
- [31] F. Zou, Y. M. Chen, K. W. Liu, Z. T. Yu, W. F. Liang, S. M. Bhaway, M. Gao, Y. Zhu, *ACS Nano* **2016**, *10*, 377.
- [32] Z. H. Li, M. F. Shao, L. Zhou, R. K. Zhang, C. Zhang, J. B. Han, M. Wei, D. G. Evans, X. Duan, *Nano Energy* **2016**, *20*, 294.
- [33] X. L. Dong, Z. Y. Guo, Y. F. Song, M. Y. Hou, J. Q. Wang, Y. G. Wang, Y. Y. Xia, *Adv. Funct. Mater.* **2014**, *24*, 3405.
- [34] Q. Sun, D. H. Kim, S. S. Park, N. Y. Lee, Y. Zhang, J. H. Lee, K. Cho, J. H. Cho, *Adv. Mater.* **2014**, *26*, 4735.
- [35] J. Ji, L. L. Zhang, H. Ji, Y. Li, X. Zhao, X. Bai, X. Fan, F. Zhang, R. S. Ruoff, *ACS Nano* **2013**, *7*, 6237.
- [36] W. Liu, C. Lu, X. Wang, K. Liang, B. K. Tay, *J. Mater. Chem. A* **2015**, *3*, 624.
- [37] G. F. Cai, J. P. Tu, J. Zhang, Y. J. Mai, Y. Lu, C. D. Gu, X. L. Wang, *Nanoscale* **2012**, *4*, 5724.
- [38] J. Luo, F. R. Fan, T. Jiang, Z. Wang, W. Tang, C. Zhang, M. Liu, G. Cao, Z. L. Wang, *Nano Res.* **2015**, *8*, 3934.
- [39] L. Lin, Y. N. Xie, S. M. Niu, S. H. Wang, P. K. Yang, Z. L. Wang, *ACS Nano* **2015**, *9*, 922.
- [40] F. Yi, L. Lin, S. Niu, P. K. Yang, Z. Wang, J. Chen, Y. Zhou, Y. Zi, J. Wang, Q. Liao, *Adv. Funct. Mater.* **2015**, *25*, 3688.